Inorganic Chemistry
Cite This: Inorg. Chem. 2018, 57, 9489−9494
Article
pubs.acs.org/IC

Nickel-4′-(3,5-dicarboxyphenyl)-2,2′,6′,2″-terpyridine Framework: Efficient Separation of Ethylene from Acetylene/Ethylene Mixtures with a High Productivity

Hui-Hong Wang,[†] Qing-Yan Liu,*[,†] Libo Li,[‡,∥] Rajamani Krishna,[§] Yu-Ling Wang,[†] Xin-Wen Peng,[†] Chun-Ting He,[†] Rui-Biao Lin,[‡] and Banglin Chen*[,‡]

[†]College of Chemistry and Chemical Engineering, Key Laboratory of Functional Small Organic Molecule of Ministry of Education, Jiangxi Normal University, Nanchang, Jiangxi 330022, P. R. China

[‡]Department of Chemistry, University of Texas at San Antonio, One UTSA Circle, San Antonio, Texas 78249-0698, United States

[§]Van't Hoff Institute for Molecular Sciences, University of Amsterdam, Science Park 904, 1098 XH Amsterdam, The Netherlands

[∥]College of Chemistry and Chemical Engineering, Taiyuan University of Technology, Taiyuan 030024, Shanxi, P. R. China

Supporting Information

ABSTRACT: A novel compound, $[Ni(DCPTP)]_n$ (termed Ni-DCPTP), based on the 4′-(3,5-dicarboxyphenyl)-2,2′,6′,2″-terpyridine ($DCPTP^{2-}$) ligand was presented here. Ni-DCPTP has a three-dimensional structure with a ths topology featuring one-dimensional (1D) helical channels. Ni-DCPTP shows an efficient removal of a trace amount of C_2H_2 from a C_2H_2/C_2H_4 (1/99) mixture with an excellent C_2H_4 productivity as demonstrated by both the transient breakthrough simulations and breakthrough experiments, generating the polymer-grade C_2H_4 gas (C_2H_2 < 40 ppm). The carboxylate oxygen atoms on the surface of 1D channels are the preferential binding sites for C_2H_2 molecules. This work demonstrates an elegant example with carboxylate oxygen-functionalized pore channels for effective C_2H_2/C_2H_4 separation.

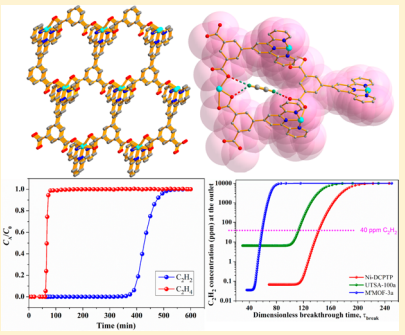

INTRODUCTION

Metal−organic frameworks (MOFs) which consist of metal ions or metal clusters and organic ligands are a unique kind of porous materials having important applications in the separation and storage of gases.[1,2] Recently, a few MOFs have been reported for the effective separation of C_2H_2 and C_2H_4.[3] Ethylene (C_2H_4), which is obtained from steam cracking in the petroleum refining process, is one of the most widely used fine chemicals. For the downstream polymerization reaction, the acetylene (C_2H_2) concentration in the C_2H_4 gas must be lower than 40 ppm (ppm), avoiding the catalyst poison during C_2H_4 polymerization.[4] Therefore, the development of porous materials for removing a trace of C_2H_2 from the C_2H_2/C_2H_4 mixture is needed. For efficient gas separation, the sieving effect and pore functionalization of the porous materials are two powerful approaches, as demonstrated in a series of MOF materials such as UTSA-100,[4] M′MOF-3a,[5] UTSA-200,[6] and SIFSIX materials.[7] For overall column breakthrough separations as evaluated by their productivity, the pore volume, framework density, gas uptake, and selectivity of C_2H_2/C_2H_4 of MOFs individually play their roles and need to be collaboratively considered. Herein the 4′-(3,5-dicarboxyphenyl)-2,2′,6′,2″-terpyridine (H_2-DCPTP) ligand with two carboxylate groups and a terpyridine was developed to construct a new MOF $[Ni(DCPTP)]_n$ (termed Ni-DCPTP). The $DCPTP^{2-}$ ligands link the Ni(II) ions to give a one-dimensional (1D) helical chain, which is further connected to its six neighbors to generate a three-dimensional (3D) framework. The Ni-DCPTP has 1D channels decorated with the carboxylate oxygen atoms, which provide the preferential binding sites for C_2H_2 molecules. The transient breakthrough simulations and transient breakthrough experiments show that Ni-DCPTP can efficiently produce the high-purity C_2H_4 from a C_2H_2/C_2H_4 (1/99) mixture under ambient conditions.

EXPERIMENTAL SECTION

Physical Measurements. The Fourier transform infrared spectrum was recorded from a KBr disc by using a PerkinElmer Spectrum One spectrometer ranging from 4000 to 400 cm^{-1}. Powder X-ray diffraction patterns were collected on a Rigaku Dmax2500 diffractometer (Cu Kα radiation, 1.5418 Å). Thermogravimetric analyses were carried out on a PE Diamond thermogravimetric analyzer under a N_2 flow. Gas sorption measurements were carried out on a Micromeritics ASAP2020 HD88 system. The highly pure N_2, C_2H_2, and C_2H_4 were used in the sorption experiments.

Breakthrough Simulations. The transient breakthrough simulations are carried out with the reported simulation methodology.[8] The detailed parameters of the breakthrough simulation are shown in the Supporting Information.

Received: May 29, 2018
Published: July 24, 2018

DOI: 10.1021/acs.inorgchem.8b01479
Inorg. Chem. 2018, 57, 9489−9494

Breakthrough Separation Experiments. The breakthrough separation experiments were performed at 298 K and 1 bar using a C_2H_2/C_2H_4 (v/v = 1/99) mixture.

Chemicals. All chemicals were purchased commercially.

Synthesis of [Ni(DCPTP)]$_n$. $Ni(CH_3COO)_2{\cdot}4H_2O$ (30.0 mg, 0.12 mmol) and 4′-(3,5-dicarboxyphenyl)-2,2′,6′,2″-terpyridine (24.0 mg, 0.06 mmol) were mixed with 3 mL of DMF and were sonicated for 5 min. Then, 0.7 mL of HNO_3 (1 M) was dropped into the above mixture. The resulting mixture was introduced into a 20 mL Parr Teflon-lined stainless-steel vessel. The sealed vessel was heated at 140 °C for 2 days and then cooled to form green crystals. The green crystals were filtered and dried. Yield: 36.7% based on 4′-(3,5-dicarboxyphenyl)-2,2′,6′,2″-terpyridine. Anal. Calcd for [Ni(DCPTP)·2DMF·H_2O]$_n$ $C_{29}H_{29}N_5O_7Ni$ (618.26): C, 56.36; H, 4.72; N, 11.29%. Found: C, 56.82; H, 4.41; N, 10.81%. IR spectrum (cm^{-1}): 3866 (w), 3742 (w), 3394 (s), 1615 (s), 1561 (s), 1474 (w), 1443 (m), 1401 (w), 1364 (s), 1319 (w), 1249 (w), 1160 (w), 1095 (w), 1052 (w), 1033 (w), 1017 (w), 879 (w), 782 (m), 751 (w), 730 (m), 663 (m), 641 (w), 421 (w).

X-ray Crystallography. Crystal data of Ni-DCPTP was collected at 293 K using a Rigaku Oxford SuperNova diffractometer (Mo Kα radiation, λ = 0.71073 Å) equipped with an Eos detector. Absorption correction and data reduction were performed using CrysAlisPro software packages.[9] The structure was solved using SHELXT[10] and refined against F^2 using SHELXTL.[11] All atoms except for hydrogens were refined with anisotropic thermal parameters. The hydrogen atoms were assigned to calculated positions and refined using a riding model. The disordered solvent molecules were treated by SQUEEZE in program PLATON[12] to give a new set of solvent-free *hkl* reflections. The structure was refined further using the solvent-free data ($R_1 = \sum||F_o| - |F_c||/\sum|F_o|$ and $wR_2 = \{\sum[w(F_o^2 - F_c^2)^2]/\sum[w(F_o^2)^2]\}^{1/2}$). The crystal data and the refinement details are summarized in Table 1.

RESULTS AND DISCUSSION

Crystal Structures. Ni-DCPTP crystallizes in the *Cc* space group and contains a $DCPTP^{2-}$ ligand and a Ni^{2+} ion in the asymmetric unit. The Ni1 ion is six-coordinated by three carboxylate O atoms from two $DCPTP^{2-}$ ligands and three N atoms of a $DCPTP^{2-}$ ligand in a distorted octahedral geometry (Figure 1a). The $DCPTP^{2-}$ ligand bridges three metal ions, showing the same coordination mode as that of the Mn(II) compound.[12] The Ni^{2+} ions are bridged by the tridentate $DCPTP^{2-}$ ligands to form a 3D framework (Figure 1b). The 3D framework features the 1D open channels running along the *b* axis (Figure 1c). Examination of the 3D framework indicated that the 1D open channels are helical channels. The Ni^{2+} ions are bridged by the $DCPTP^{2-}$ ligands to form two kinds of helixes with opposite chirality (Figure S1 in Supporting Information). Topologically, the Ni^{2+} ion is a 3-connected node, and the $DCPTP^{2-}$ ligand bridges three metal ions serving as a 3-connected node. It is interesting that the two types of 3-connected nodes are topologically equivalent nodes. Thus, the 3D framework is the (10, 3)-d (ths) topological net with the Schläfli symbol ($10_2{\cdot}10_4{\cdot}10_4$). Such a network contains the alternate arrangement of the parallel left- and right-handed helical chains in a mole ratio of 1:1, which in Ni-DCPTP alternates along the *c* axis (Figure S2). The disordered DMF and water solvent molecules, which account for 46.7% of the unit cell volume,[13] fill the 1D channels with a diameter of about 10 Å.

Table 1. Crystallographic Data for Ni-DCPTP[a]

formula	$C_{23}H_{13}N_3O_4Ni$
fw	454.07
temp (K)	293(2)
cryst syst	monoclinic
space group	*Cc*
Z	4
a (Å)	18.3324(10)
b (Å)	8.4996(5)
c (Å)	20.0672(12)
α (deg)	90
β (deg)	107.688(6)
γ (deg)	90
V (Å^3)	2979.0(3)
D_{calcd} (g cm^{-3})	1.012
μ (mm^{-1})	0.676
no. of reflns collected	14705
independent reflns	5956
obsd reflns ($I > 2\sigma(I)$)	5366
F(000)	928
R[int]	0.0560
R_1 ($I > 2\sigma(I)$)	0.0474
wR_2 (all data)	0.1431
CCDC number	1842691

[a] $R_1 = \sum||F_o| - |F_c||/\sum|F_o|$ and $wR_2 = \{\sum[w(F_o^2 - F_c^2)^2]/\sum[w(F_o^2)^2]\}^{1/2}$.

Gas Adsorption Properties. As mentioned above, Ni-DCPTP has 1D pore channels. The porous character of Ni-DCPTP was demonstrated by N_2 adsorption experiments at 77 K. The as-synthesized Ni-DCPTP was exchanged with CH_2Cl_2 several times and then exchanged with dry *n*-hexane several times before thermal activation at 120 °C under a dynamic vacuum. Removal of solvent molecules from the framework was observed below 115 °C, as shown by the TGA curve of the solvent-exchanged sample (Figure S3). The N_2 sorption isotherm of Ni-DCPTP displays a characteristic reversible type I isotherm featuring a sharp uptake at $P/P° < 0.01$ (Figure 2). The N_2 uptake for Ni-DCPTP at 1 atm is 281 cm^3 (STP) g^{-1}, suggesting the microporous structure of Ni-DCPTP. The Langmuir and Brunauer–Emmett–Teller surface areas for Ni-DCPTP are 1229 and 857 m^2 g^{-1}, respectively. The total pore volume of 0.428 cm^3 g^{-1} derived from the N_2 adsorption isotherm matches well with the estimated value (0.461 cm^3 g^{-1}) from the crystal data. The narrow distribution of micropores around 6.7 and 10 Å (Figure 2, inset) was provided by the nonlocal density functional theory model based on the N_2 adsorption data. PXRD of the sample after adsorption matches well with the pristine one, suggesting the maintenance of the 3D framework after adsorption (Figure S4).

To value its potential for gas separation, the gas sorption isotherms of C_2H_2 and C_2H_4 at 273 and 298 K for Ni-DCPTP were collected. At 273 K and 1 atm, C_2H_2 and C_2H_4 uptake amounts for Ni-DCPTP are 173.6 and 116.8 cm^3 g^{-1}, respectively (Figure 3a), indicating that the C_2H_2 uptake of Ni-DCPTP is high. At 298 K and 1 atm, Ni-DCPTP takes up 146.4 cm^3 g^{-1} of C_2H_2 and 100.4 cm^3 g^{-1} of C_2H_4 (Figure 3b). At 298 K, the C_2H_2/C_2H_4 uptake ratio of 1.46 for Ni-DCPTP is higher than those of the MOF-74 series.[14] Though the C_2H_2/C_2H_4 uptake ratio for Ni-DCPTP is smaller than those of UTSA-100a (2.57)[4] and M′MOF-3a (4.75),[5] the C_2H_2 uptake (6.53 mmol g^{-1}) for Ni-DCPTP at 298 K is much higher than those of the UTSA-100a (4.27 mmol g^{-1}) and M′MOF-3a (1.9 mmol g^{-1}) at 296 K. It should be noted that Ni-DCPTP rapidly adsorbs C_2H_2 at low pressure with C_2H_2 uptake reaching 105.8 cm^3 g^{-1} (298 K) and 142.2 cm^3 g^{-1}

DOI: 10.1021/acs.inorgchem.8b01479
Inorg. Chem. 2018, 57, 9489–9494

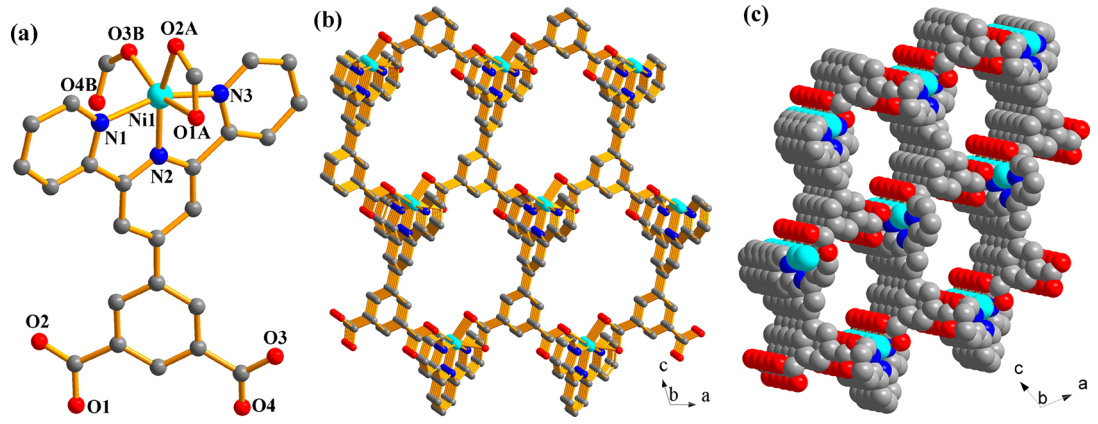

Figure 1. (a) Coordinated environment of Ni atom, (b) 3D framework, and (c) 1D pore channel of Ni-DCPTP.

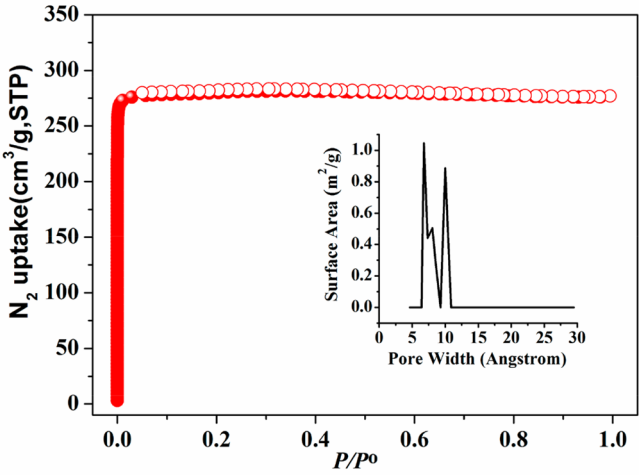

Figure 2. N_2 absorption/desorption isotherms of Ni-DCPTP at 77 K.

(273 K) at 155 mm Hg, while the C_2H_4 uptakes at 155 mm Hg are 66.1 $cm^3\ g^{-1}$ (298 K) and 93.2 $cm^3\ g^{-1}$ (273 K). Such a dramatic difference between C_2H_2 and C_2H_4 uptakes indicates that Ni-DCPTP is very promising for C_2H_2/C_2H_4 separation. The ideal adsorbed solution theory (IAST) calculation gives the C_2H_2/C_2H_4 (1/99) adsorption selectivity of 5.5 at 1 kPa (Figure S5). The C_2H_2/C_2H_4 adsorption selectivity is greater than those of Fe-MOF-74 (2.1)[14a] and NOTT-300 (2.2–2.5).[3d] Fitting of the adsorption isotherms at 273 and 298 K with the virial method gives the isosteric heat of adsorption Q_{st} for C_2H_2 in the range 38.9–39.4 kJ mol^{-1} (Figure S6), which is comparable to those of SIFSIX-2-Cu-i (42.0 kJ mol^{-1})[7a] and Fe-MOF-74 (46.5 kJ mol^{-1}).[14a] As shown in Figure 1c, the 1D channels are decorated by the carboxylate oxygen atoms, especially for the uncoordinated carboxylate oxygen atoms, which will provide basic binding sites for the C_2H_2 molecules. Additionally, the PXRD pattern of the Ni-DCPTP sample after exposure to air for 20 h remained unchanged (Figure S4), indicating the Ni-DCPTP material is stable in atmospheric moisture. The C_2H_2 and C_2H_4 adsorption curves at 298 K for Ni-DCPTP after exposure to air for 20 h overlap with the corresponding adsorption curves for the pristine Ni-DCPTP (Figure S7). Such a result indicates that the C_2H_2 and C_2H_4 adsorptions are not affected by a trace of water.

Dynamic Separation of C_2H_2/C_2H_4 Gas Mixtures. For evaluation of the C_2H_2/C_2H_4 separation performances for Ni-DCPTP, we performed transient breakthrough simulations[15] in column adsorption processes for Ni-DCPTP and other MOFs. For mimicking the actual industrial process, the C_2H_2/C_2H_4 mixture (1/99) was used as a feed. Figure 4 demonstrates the dimensionless time (τ)-dependent molar concentrations of C_2H_2/C_2H_4 at the outlet of the adsorber packed with the studied MOFs at 100 kPa and 298 K. The C_2H_4 eluted through the bed first to produce a polymer-grade C_2H_4, and then C_2H_2 broke through from the bed at a certain time τ_{break}, indicating that a clean separation was realized (Figure 4). The dimensionless τ_{break} value for Ni-DCPTP is significant larger

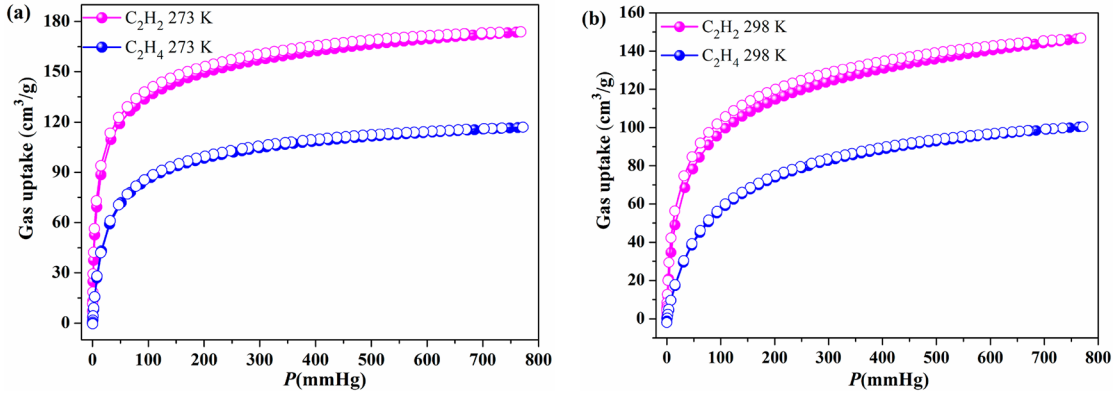

Figure 3. Acetylene (magenta) and ethylene (blue) sorption isotherms of Ni-DCPTP (a) at 273 K and (b) at 298 K. (The closed and open symbols represent the adsorption and desorption curves, respectively.)

DOI: 10.1021/acs.inorgchem.8b01479
Inorg. Chem. 2018, 57, 9489–9494

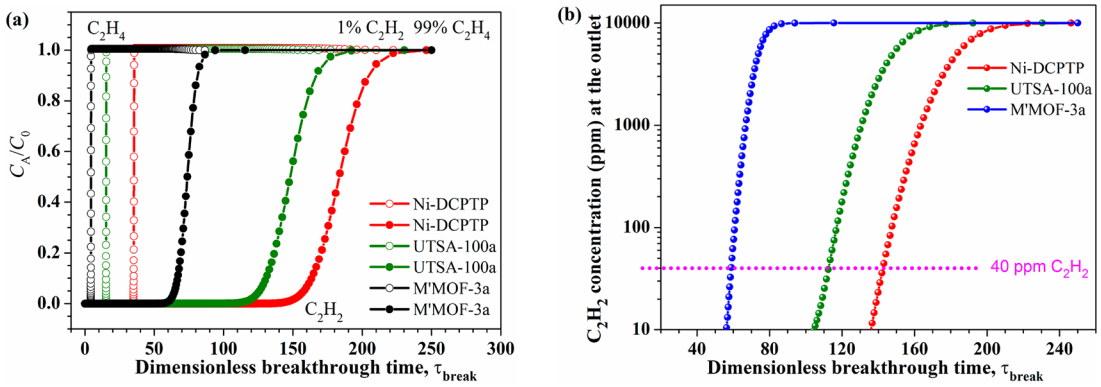

Figure 4. (a) Simulated column breakthrough curves for C_2H_2/C_2H_4 separation for MOFs as indicated (C_2H_2 and C_2H_4 are represented as open circles and filled circles, respectively; C_A/C_0, outlet concentration/feed concentration). (b) C_2H_2 concentration at the outlet versus τ_{break} for MOFs.

than those of the MOFs we studied (Figure 4a,b). The amount of purified C_2H_4 (containing <40 ppm of C_2H_2) produced by Ni-DCPTP during the $0-\tau_{break}$ time interval was determined to be 12.9 mol L^{-1}. The data on C_2H_4 productivity for Ni-DCPTP material exceeds those of USTA-100a and M′MOF-3a (Figure 5). In general, the C_2H_4 separation productivity from

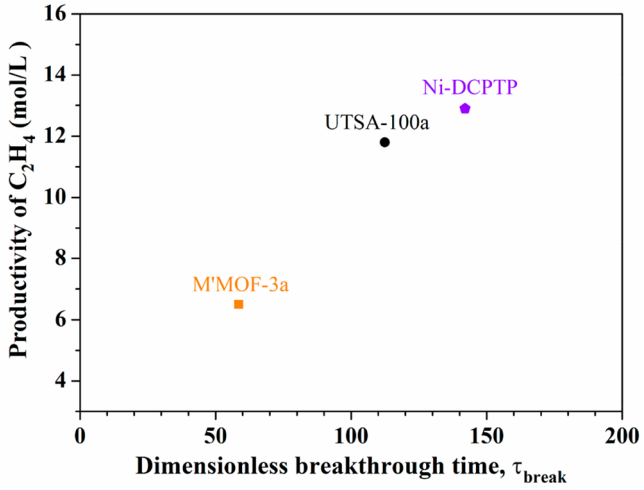

Figure 5. C_2H_4 productivity versus τ_{break} for Ni-DCPTP, UTSA-100a, and M′MOF-3a.

the C_2H_2/C_2H_4 gas mixture is dependent on the pore volume, the framework density, the uptakes of C_2H_2 and C_2H_4, and the selectivity of C_2H_2/C_2H_4. As shown in Table 2, though the M′MOF-3a has the highest selectivity and low framework density, the C_2H_4 productivity is still the lowest due to its relatively low uptake of C_2H_2 and pore volume, which restrict its separation performance. The Ni-DCPTP has the highest uptake of C_2H_2 and pore volume, and moderate selectivity of C_2H_2/C_2H_4, which displays the highest C_2H_4 productivity. Thus, the Ni-DCPTP material demonstrates an efficient removal of trace of C_2H_2 from C_2H_4 gas (1/99 mixture) with an excellent C_2H_4 productivity.

To assess the actual separation performance of Ni-DCPTP, the dynamic gas breakthrough was measured. A sample of Ni-DCPTP was exposed to a 2 mL min^{-1} flow rate of a C_2H_2/C_2H_4 (v/v = 1/99) gas mixture at 298 K. C_2H_4 first eluted through the packed column in a high-purity grade (Figure 6), while C_2H_2 was kept in an adsorber over 330 min. The time

Table 2. Summary of the Adsorption Data for Acetylene and Ethylene in Representative MOFs

	Ni-DCPTP	UTSA-100a	M′MOF-3a
surface area (m^2 g^{-1}; BET)	857	970	110
pore volume (cm^3 g^{-1})	0.428	0.399	0.165
framework density (kg m^{-3})	1012	1146	1023
C_2H_2 uptake at 100 kPa (cm^3 g^{-1})	146.4[d]	95.6[e]	42.6[f]
C_2H_4 uptake at 100 kPa (cm^3 g^{-1})	100.4[d]	37.2[e]	8.96[f]
C_2H_2/C_2H_4 uptake ratio	1.46	2.57	4.75
selectivity for C_2H_2/C_2H_4[a]	5.5	10.72	24.03
Q_{st} (C_2H_2, kJ mol^{-1})[b]	38.9	22.1	25
C_2H_4 productivity (mol L^{-1})[c]	12.9	11.8	6.6

[a]IAST analysis for ethylene/acetylene mixtures containing 1% acetylene at 100 kPa. [b]Q_{st} values at low surface coverage. [c]C_2H_2/C_2H_4 mixture (1/99) and the purified C_2H_4 containing <40 ppm of C_2H_2. [d]At 298 K. [e]At 296 K. [f]At 295 K.

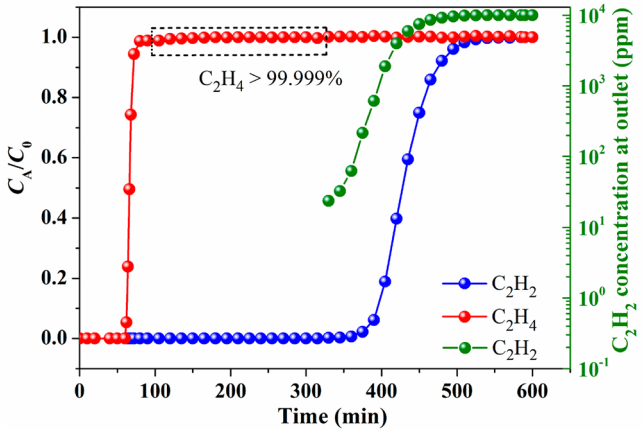

Figure 6. Experimental column breakthrough curves for the C_2H_2/C_2H_4 (v/v = 1/99) mixture on Ni-DCPTP at 298 K.

determined by gas chromatography is up to 315 min for the C_2H_4 outlet effluent with the C_2H_2 concentration below 10 ppm (Figure 6), affording a high C_2H_4 purity of >99.999%. Obviously, Ni-DCPTP can remove the trace of C_2H_2 from C_2H_4 gas and provide the polymer-grade C_2H_4 gas. During the breakthrough process, the C_2H_2-captured amount was analyzed to be 174 mmol L^{-1}. The C_2H_4 productivity for Ni-DCPTP calculated from the experimental breakthrough curves is 12.1 mol L^{-1}.

DOI: 10.1021/acs.inorgchem.8b01479
Inorg. Chem. 2018, 57, 9489−9494

In order to uncover the gas separation mechanism of Ni-DCPTP, detailed computational investigations were performed (Supporting Information). First, grand canonical Monte Carlo (GCMC) simulations give the preferential adsorption sites of C_2H_2 and C_2H_4 located between two pyridine and two benzene rings connected by weak interactions with the host frameworks, respectively. Further density functional theory (DFT-D) calculations reveal that C_2H_2 can form a strong hydrogen bond (C−H···O = 3.538 Å with H···O = 2.468 Å) with the uncoordinated carboxylate O atom as well as two pthers (C−H···O = 3.545 and 4.160 Å with H···O = 2.723 and 3.098 Å) with other two coordinated carboxylate O atoms (Figure 7). In contrast, only a weak hydrogen bond (C−H···O = 4.016 Å with a H···O = 2.938 Å) between C_2H_4 and coordinated carboxylate O atom and weak C−H···π (H···π = 3.089, 3.689, and 3.356 Å) interactions between C_2H_4 and framework are observed (Figure S8). Thus, C_2H_2 exhibits a large binding energy of −64.1 kJ/mol while a small binding energy of −56.6 kJ/mol is observed for C_2H_4.

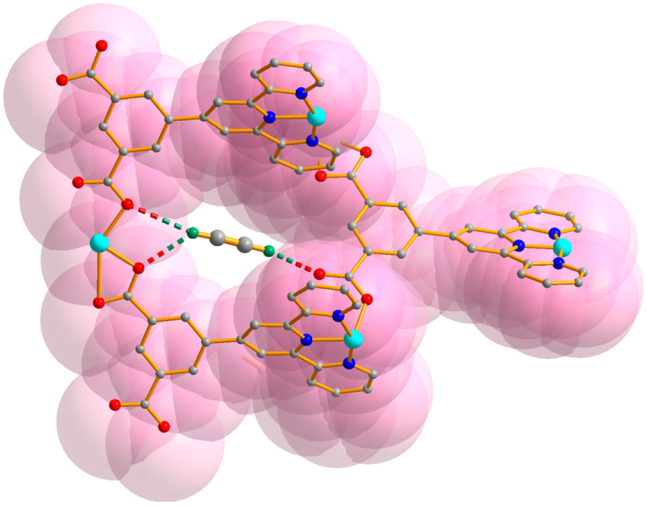

Figure 7. Preferential binding sites for C_2H_2 adsorption in Ni-DCPTP.

CONCLUSIONS

In summary, a nickel(II) compound based on the 4′-(3,5-dicarboxyphenyl)-2,2′,6′,2″-terpyridine ($DCPTP^{2-}$) ligand with the carboxylate O and pyridine N donors is presented here. The porous compound of Ni-DCPTP has a 3D framework containing two kinds of helical chains with opposite chirality. Ni-DCPTP efficiently removes the trace of C_2H_2 from the C_2H_2/C_2H_4 mixture with a high C_2H_4 productivity, which is confirmed by the transient breakthrough simulations and the actual column breakthrough experiments. The result of the computational calculations demonstrates that the basic adsorption site for C_2H_2 in Ni-DCPTP is the carboxylate oxygen atoms on the surface of the 1D channels. This work presents an elegant example with carboxylate oxygen-functionalized pore channels for effective C_2H_2/C_2H_4 separation.

ASSOCIATED CONTENT

Supporting Information

The Supporting Information is available free of charge on the ACS Publications website at DOI: 10.1021/acs.inorgchem.8b01479.

Crystal structure, PXRD patterns, TG curves, C_2H_2/C_2H_4 adsorption selectivity, Q_{st} of C_2H_2 and C_2H_4 adsorption, and detailed computational calculations (PDF)

Accession Codes

CCDC 1842691 contains the supplementary crystallographic data for this paper. These data can be obtained free of charge via www.ccdc.cam.ac.uk/data_request/cif, or by emailing data_request@ccdc.cam.ac.uk, or by contacting The Cambridge Crystallographic Data Centre, 12 Union Road, Cambridge CB2 1EZ, UK; fax: +44 1223 336033.

AUTHOR INFORMATION

Corresponding Authors

*E-mail: qyliuchem@jxnu.edu.cn. Fax: +86-791-88336372. (Q.-Y.L.)

*E-mail: banglin.chen@utsa.edu. (B.C.)

ORCID

Qing-Yan Liu: 0000-0003-1991-792X

Rajamani Krishna: 0000-0002-4784-8530

Yu-Ling Wang: 0000-0002-0839-699X

Rui-Biao Lin: 0000-0003-3267-220X

Banglin Chen: 0000-0001-8707-8115

Notes

The authors declare no competing financial interest.

ACKNOWLEDGMENTS

The authors acknowledge the NNSFC (21561015 and 21661014), the key project of NSF of Jiangxi Province (20171ACB20008), and the Welch Foundation (AX-1730) for financial support.

REFERENCES

(1) (a) Furukawa, H.; Cordova, K. E.; O'Keeffe, M.; Yaghi, O. M. The Chemistry and Applications of Metal-Organic Frameworks. *Science* **2013**, *341*, 974−975. (b) Chen, B.; Xiang, S.; Qian, G. Metal-Organic Frameworks with Functional Pores for Recognition of Small Molecules. *Acc. Chem. Res.* **2010**, *43*, 1115−1124. (c) Cui, Y.; Li, B.; He, H.; Zhou, W.; Chen, B.; Qian, G. Metal-Organic Frameworks as Platforms for Functional Materials. *Acc. Chem. Res.* **2016**, *49*, 483−493. (d) Li, B.; Chrzanowski, M.; Zhang, Y.; Ma, S. Applications of metal-organic frameworks featuring multi-functional sites. *Coord. Chem. Rev.* **2016**, *307*, 106−129. (e) Zhu, Q.-L.; Xu, Q. Metal-organic framework composites. *Chem. Soc. Rev.* **2014**, *43*, 5468−5512. (f) Wang, H.; Yao, K.; Zhang, Z.; Jagiello, J.; Gong, Q.; Han, Y.; Li, J. The first example of commensurate adsorption of atomic gas in a MOF and effective separation of xenon from other noble gases. *Chem. Sci.* **2014**, *5*, 620−624.

(2) (a) Li, J.-R.; Kuppler, R. J.; Zhou, H.-C. Selective gas adsorption and separation in metal-organic frameworks. *Chem. Soc. Rev.* **2009**, *38*, 1477−1504. (b) Wang, C.; Liu, D.; Lin, W. Metal-Organic Frameworks as A Tunable Platform for Designing Functional Molecular Materials. *J. Am. Chem. Soc.* **2013**, *135*, 13222−13234. (c) Liao, P.-Q.; Huang, N.-Y.; Zhang, W.-X.; Zhang, J.-P.; Chen, X.-M. Controlling guest conformation for efficient purification of butadiene. *Science* **2017**, *356*, 1193−1196. (d) Gao, W. Y.; Tsai, C. Y.; Wojtas, L.; Thiounn, T.; Lin, C. C.; Ma, S. Q. Interpenetrating Metal-Metalloporphyrin Framework for Selective CO_2 Uptake and Chemical Transformation of CO_2. *Inorg. Chem.* **2016**, *55*, 7291−7294. (e) Zhao, X.; Wang, Y.; Li, D.-S.; Bu, X.; Feng, P. Metal-Organic Frameworks for Separation. *Adv. Mater.* **2018**, 1705189. (f) Ye, Y.; Xiong, S.; Wu, X.; Zhang, L.; Li, Z.; Wang, L.; Ma, X.; Chen, Q.-H.; Zhang, Z.; Xiang, S. Microporous Metal−Organic Framework Stabilized by Balanced Multiple Host−Couteranion Hydrogen-

DOI: 10.1021/acs.inorgchem.8b01479
Inorg. Chem. 2018, 57, 9489−9494

Bonding Interactions for High-Density CO_2 Capture at Ambient Conditions. *Inorg. Chem.* **2016**, *55*, 292−299.
(3) (a) Bao, Z.-B.; Chang, G.-G.; Xing, H.-B.; Krishna, R.; Ren, Q.-L.; Chen, B.-L. Potential of microporous metal-organic frameworks for separation of hydrocarbon mixtures. *Energy Environ. Sci.* **2016**, *9*, 3612−3641. (b) Cadiau, A.; Adil, K.; Bhatt, P. M.; Belmabkhout, Y.; Eddaoudi, M. A metal-organic framework-based splitter for separating propylene from propane. *Science* **2016**, *353*, 137−140. (c) Li, L.; Lin, R.-B.; Krishna, R.; Wang, X.; Li, B.; Wu, H.; Li, J.; Zhou, W.; Chen, B. Flexible-Robust Metal-Organic Framework for Efficient Removal of Propyne from Propylene. *J. Am. Chem. Soc.* **2017**, *139*, 7733−7736. (d) Yang, S.-H.; Ramirez-Cuesta, A. J.; Newby, R.; Garcia-Sakai, V.; Manuel, P.; Callear, S. K.; Campbell, S. I.; Tang, C. C.; Schröder, M. Supramolecular binding and separation of hydrocarbons within a functionalized porous metal-organic framework. *Nat. Chem.* **2015**, *7*, 121−129. (e) Yao, Z.; Zhang, Z.; Liu, Z.; Li, L.; Zhou, W.; Zhao, Y.; Han, Y.; Chen, B.; Krishna, R.; Xiang, S. Extraordinary Separation of Acetylene-Containing Mixtures with Microporous Metal−Organic Frameworks with Open O Donor Sites and Tunable Robustness through Control of the Helical Chain Secondary Building Units. *Chem. - Eur. J.* **2016**, *22*, 5676−5683.
(4) Hu, T.-L.; Wang, H.; Li, B.; Krishna, R.; Wu, H.; Zhou, W.; Zhao, Y.; Han, Y.; Wang, X.; Zhu, W.; Yao, Z.; Xiang, S.; Chen, B. Microporous metal-organic framework with dual functionalities for highly efficient removal of acetylene from ethylene/acetylene mixtures. *Nat. Commun.* **2015**, *6*, 7328.
(5) Xiang, S.-C.; Zhang, Z.; Zhao, C.-G.; Hong, K.; Zhao, X.; Ding, D.-R.; Xie, M.-H.; Wu, C.-D.; Das, M. C.; Gill, R.; Thomas, K. M.; Chen, B. Rationally tuned micropores within enantiopure metal-organic frameworks for highly selective separation of acetylene and ethylene. *Nat. Commun.* **2011**, *2*, 204.
(6) (a) Li, B.; Cui, X.-L.; O'Nolan, D.; Wen, H.-M.; Jiang, M.-D.; Krishna, R.; Wu, H.; Lin, R.-B.; Chen, Y.-S.; Yuan, D.-Q.; Xing, H.-B.; Zhou, W.; Ren, Q.-L.; Qian, G.-D.; Zaworotko, M. J.; Chen, B. An Ideal Molecular Sieve for Acetylene Removal from Ethylene with Record Selectivity and Productivity. *Adv. Mater.* **2017**, *29*, 1704210.
(7) (a) Cui, X.; Chen, K.; Xing, H.; Yang, Q.; Krishna, R.; Bao, Z.; Wu, H.; Zhou, W.; Dong, X.; Han, Y.; Li, B.; Ren, Q.; Zaworotko, M. J.; Chen, B. Pore chemistry and size control in hybrid porous materials for acetylene capture from ethylene. *Science* **2016**, *353*, 141−144. (b) Nugent, P.; Belmabkhout, Y.; Burd, S. D.; Cairns, A. J.; Luebke, R.; Forrest, K.; Pham, T.; Ma, S.-Q.; Space, B.; Wojtas, L.; Eddaoudi, M.; Zaworotko, M. J. Porous materials with optimal adsorption thermodynamics and kinetics for CO_2 separation. *Nature* **2013**, *495*, 80−84. (c) Burd, S. D.; Ma, S.; Perman, J. A.; Sikora, B. J.; Snurr, R. Q.; Thallapally, P. K.; Tian, J.; Wojtas, L.; Zaworotko, M. J. Highly Selective Carbon Dioxide Uptake by $[Cu(bpy\text{-}n)_2(SiF_6)]$ (bpy-1 = 4,4'-Bipyridine; bpy-2 = 1,2-Bis(4-pyridyl)ethene). *J. Am. Chem. Soc.* **2012**, *134*, 3663−3666. (d) Lin, R.-B.; Li, L.; Wu, H.; Arman, H.; Li, B.; Lin, R.-G.; Zhou, W.; Chen, B. Optimized Separation of Acetylene from Carbon Dioxide and Ethylene in a Microporous Material. *J. Am. Chem. Soc.* **2017**, *139*, 8022−8028.
(8) Krishna, R. The Maxwell-Stefan Description of Mixture Diffusion in Nanoporous Crystalline Materials. *Microporous Mesoporous Mater.* **2014**, *185*, 30−50.
(9) *CrysAlisPro*; Rigaku Oxford Diffraction: The Woodlands, TX, 2015.
(10) Sheldrick, G. M. SHELXT−Integrated space-group and crystal-structure determination. *Acta Crystallogr., Sect. A: Found. Adv.* **2015**, *A71*, 3−8.
(11) Sheldrick, G. M. Crystal structure refinement with SHELXL. *Acta Crystallogr., Sect. C: Struct. Chem.* **2015**, *C71*, 3−8.
(12) Bai, N.-N.; Hou, L.; Gao, R.-C.; Liang, J.-Y.; Yang, F.; Wang, Y.-Y. Five 1D to 3D Zn(II)/Mn(II)-CPs based on dicarboxyphenyl-terpyridine ligand: stepwise adsorptivity and magnetic properties. *CrystEngComm* **2017**, *19*, 4789−4796.
(13) Spek, A. L. *PLATON: A Multipurpose Crystallographic Tool*; Utrecht University: Utrecht, The Netherlands, 2001.
(14) (a) Bloch, E. D.; Queen, W. L.; Krishna, R.; Zadrozny, J. M.; Brown, C. M.; Long, J. R. Hydrocarbon separations in a metal-organic framework with open iron(II) coordination sites. *Science* **2012**, *335*, 1606−1610. (b) He, Y.; Krishna, R.; Chen, B. Metal-organic frameworks with potential for energy-efficient adsorptive separation of light hydrocarbons. *Energy Environ. Sci.* **2012**, *5*, 9107−9120.
(15) Krishna, R. Methodologies for Evaluation of Metal-Organic Frameworks in Separation Applications. *RSC Adv.* **2015**, *5*, 52269−52295.

DOI: 10.1021/acs.inorgchem.8b01479
Inorg. Chem. 2018, 57, 9489−9494

Nickel-4′-(3,5-Dicarboxyphenyl)-2,2′,6′,2′′-terpyridine Framework: Efficient Separation of Ethylene from Acetylene/Ethylene Mixtures with a High Productivity

Hui-Hong Wang,[†] Qing-Yan Liu *,[†] Libo Li,[‡,#] Rajamani Krishna,[§] Yu-Ling Wang,[†] Xin-Wen Peng,[†] Chun-Ting He,[†] Rui-Biao Lin,[‡] and Banglin Chen *,[‡]

[†]*College of Chemistry and Chemical Engineering, Key Laboratory of Functional Small Organic Molecule of Ministry of Education, Jiangxi Normal University, Nanchang 330022, P. R. China.*

[‡] *Department of Chemistry, University of Texas at San Antonio, One UTSA Circle, San Antonio, Texas 78249-0698, United States.*

[§]*Van't Hoff Institute for Molecular Sciences, University of Amsterdam, Science Park 904, 1098 XH Amsterdam, The Netherlands.*

[#] *College of Chemistry and Chemical Engineering, Taiyuan University of Technology, Taiyuan 030024, Shanxi, P. R. China*

Supporting Information

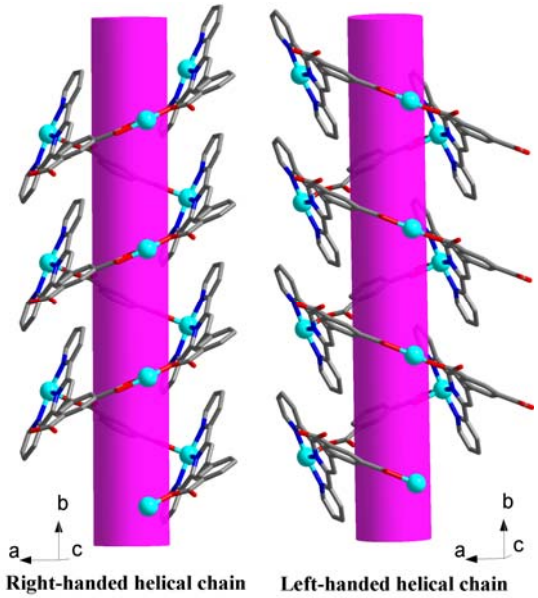

Figure S1. The helical chains in Ni-DCPTP.

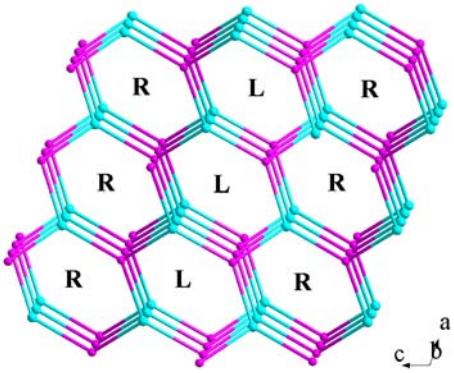

Figure S2. Schematic representation of the 3-connected (10,3)-d topological net of Ni-DCPTP (L = left-handed chain and R = right-handed chain).

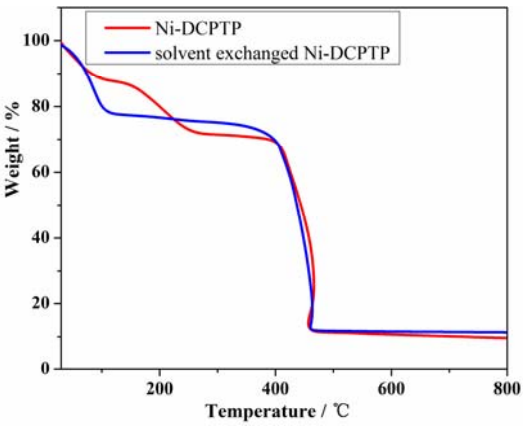

Figure S3. TGA curves for Ni-DCPTP.

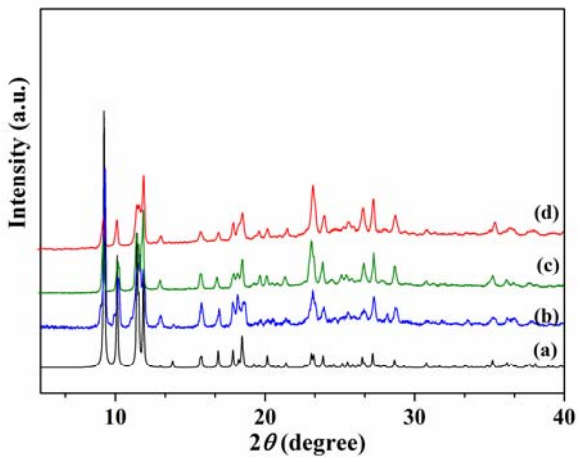

Figure S4. PXRD patterns for Ni-DCPTP (a) Simulated, (b) Experimental, (c) After exposure to air 20 h, and (d) After adsorption.

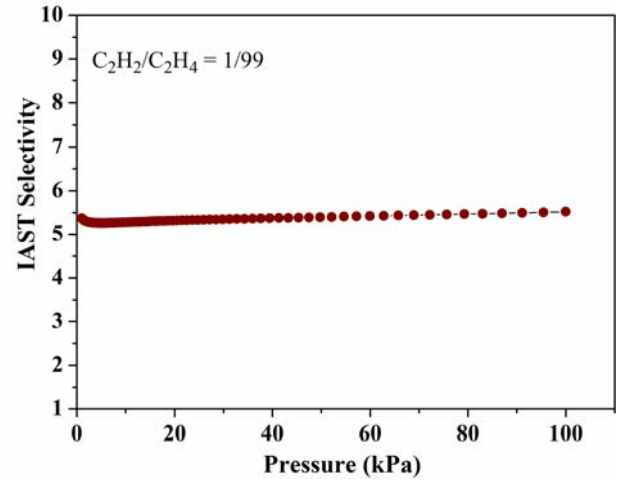

Figure S5. IAST calculations of the C_2H_2/C_2H_4 adsorption selectivity for Ni-DCPTP.

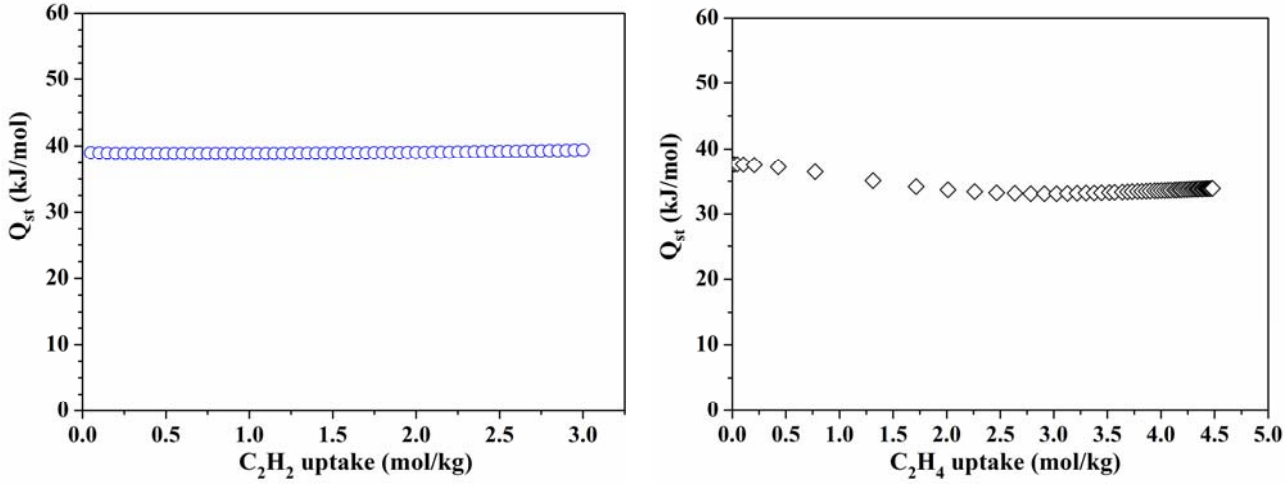

Figure S6. The Q_{st} of C_2H_2 and C_2H_4 adsorption for Ni-DCPTP.

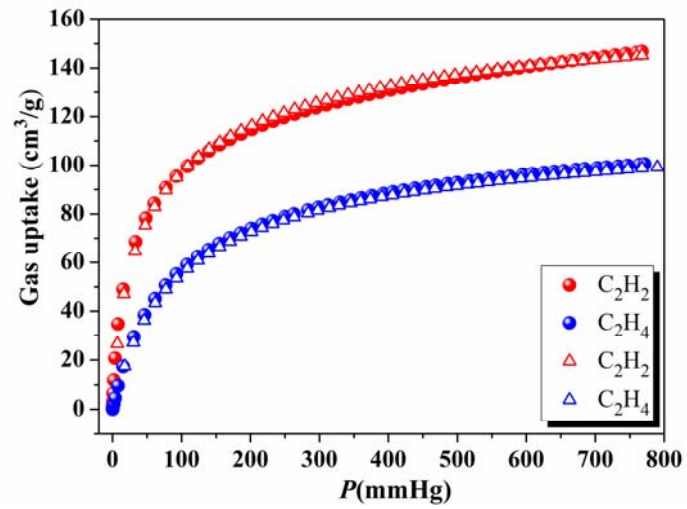

Figure S7. The C_2H_2 and C_2H_4 adsorption curves at 298 K for the as-synthesized Ni-DCPTP (closed circles) and the Ni-DCPTP after exposure to air for 20 h (open triangle).

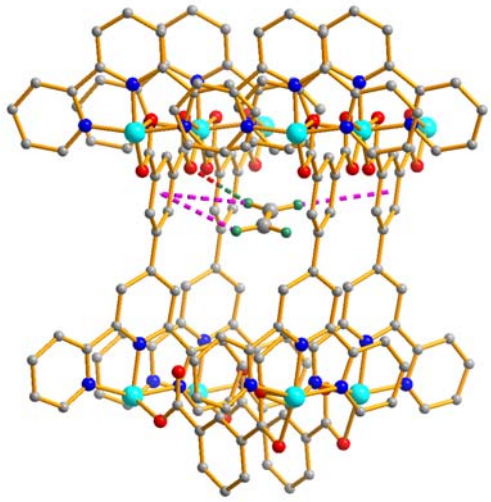

Figure S8. DFT-D-calculated the preferential binding sites for C_2H_4 adsorption in Ni-DCPTP.

Breakthrough simulations. The performance of industrial fixed bed adsorbers is dictated by a combination of adsorption selectivity and uptake capacity. For a proper evaluation of Ni-DCPTP and other MOFs we performed transient breakthrough simulations. A brief description of the simulation methodology is provided below.

Assuming plug flow of an *n*-component gas mixture through a fixed bed maintained under isothermal, isobaric, conditions, the molar concentrations in the gas phase at any position and instant of time are obtained by solving the following set of partial differential equations for each of the species *i* in the gas mixture.[1]

$$\frac{\partial c_i(t,z)}{\partial t}+\frac{\partial\left(v(t,z)c_i(t,z)\right)}{\partial z}+\frac{\left(1-\varepsilon\right)}{\varepsilon}\rho\frac{\partial \bar{q}_i(t,z)}{\partial t}=0;\quad i=1,2,...n \tag{1}$$

In equation (1), t is the time, z is the distance along the adsorber, ρ is the framework density, ε is the bed voidage, v is the interstitial gas velocity, and $\bar{q}_i(t,z)$ is the *spatially averaged* molar loading within the crystallites of radius r_c, monitored at position z, and at time t. The time $t = 0$, corresponds to the time at which the feed mixture is injected at the inlet to the fixed bed. Prior to injection of the feed, it is assumed that an inert, non-adsorbing, gas flows through the fixed bed.

At any time t, during the transient approach to thermodynamic equilibrium, the spatially averaged molar loading within the crystallite r_c is obtained by integration of the radial loading profile

$$\bar{q}_i(t)=\frac{3}{r_c^3}\int_0^{r_c}q_i(r,t)r^2dr \tag{2}$$

If the value of intra-crystalline diffusivities are large enough to ensure that intra-crystalline gradients are absent, the entire crystallite particle can be considered to be in thermodynamic equilibrium with the surrounding bulk gas phase at that time t, and position z of the adsorber

$$\bar{q}_i(t,z)=q_i(t,z) \tag{3}$$

The molar loadings at the *outer surface* of the crystallites, i.e. at $r = r_c$, are calculated on the basis of adsorption equilibrium with the bulk gas phase partial pressures p_i at that position z and time t. The adsorption equilibrium are calculated on the basis of the IAST description of mixture adsorption equilibrium.

The *interstitial* gas velocity is related to the *superficial* gas velocity by

$$v=\frac{u}{\varepsilon} \tag{4}$$

The adsorber bed is assumed to be initially free of adsorbates, i.e. we have the initial condition

$$t=0;\quad q_i(0,z)=0 \tag{5}$$

At time, $t = 0$, the inlet to the adsorber, $z = 0$, is subjected to a step input of the n-component gas mixture and this step input is maintained till the end of the adsorption cycle when steady-state conditions are reached.

$$t\geq 0;\quad p_i(0,t)=p_{i0};\quad u(0,t)=u_0 \tag{6}$$

where $u_0=v_0\varepsilon$ is the superficial gas velocity at the inlet to the adsorber.

For the breakthrough simulations, the following parameter values were used: length of packed bed,

L = 0.12 m; voidage of packed bed, ε = 0.75; interstitial gas velocity at inlet, v = 0.003 m/s. The transient breakthrough simulation results are presented in terms of a *dimensionless* time, τ, defined by dividing the actual time, t, by the characteristic time, $\frac{L}{v}$.

In the breakthrough simulations with all MOFs, the total bulk gas phase is at 298 K and 100 kPa; the partial pressures of C_2H_2, and C_2H_4 in the inlet feed gas mixture are, respectively, p_1 = 1 kPa, p_2 = 99 kPa. On the basis of the gas phase concentrations exiting the fixed bed, we can calculate the impurity level of C_2H_2 in the gas mixture exiting the fixed bed packed with different MOFs (Figure 4b).

At a certain time, τ_{break}, the impurity level will exceed the desired purity level of 40 ppm that corresponds to the purity requirement of the feed to the polymerization reactor. The adsorption cycle needs to be terminated at that time τ_{break} and the regeneration process needs to be initiated. From a material balance on the adsorber, the amount of purified C_2H_4 produced (containing < 40 ppm C_2H_2) during the time interval $0-\tau_{break}$ can be determined. The calculations of the productivity of pure C_2H_4 produced (containing < 40 ppm C_2H_2) in the gas phase exiting the adsorber are performed using the computer code that solves the set of partial differential equation (1). The values of the productivity of pure C_2H_4, expressed in mol C_2H_4 per L of adsorbent is provided in Table S1. The hierarchy of productivities is directly related to the corresponding hierarchy of breakthrough times, τ_{break}.

Furthermore, during the time interval $0-\tau_{break}$, the amount of C_2H_2 that is captured (i.e. adsorbed in the MOF crystal) can also be determined from a material balance using the computer code that solves the set of partial differential equation (1). The values of the capture capacity of C_2H_2, expressed in mmol C_2H_2 per L of adsorbent, is also provided in Table S1.

Breakthrough separation experiments. The breakthrough curves were measured on a homemade apparatus for gases mixtures C_2H_2/C_2H_4 (v/v = 1/99) at 298 K and 1 bar. The gas flows were controlled at the inlet by a mass flow meter as 2 mL min^{-1}, and a gas chromatograph (TCD-Thermal Conductivity Detector) continuously monitored the effluent gas from the adsorption bed. Prior to every breakthrough experiment, we activated the sample by flushing the adsorption bed with helium gas for 1 hours at 298 K. Subsequently, the column was allowed to equilibrate at the measurement rate before we switched the gas flow.

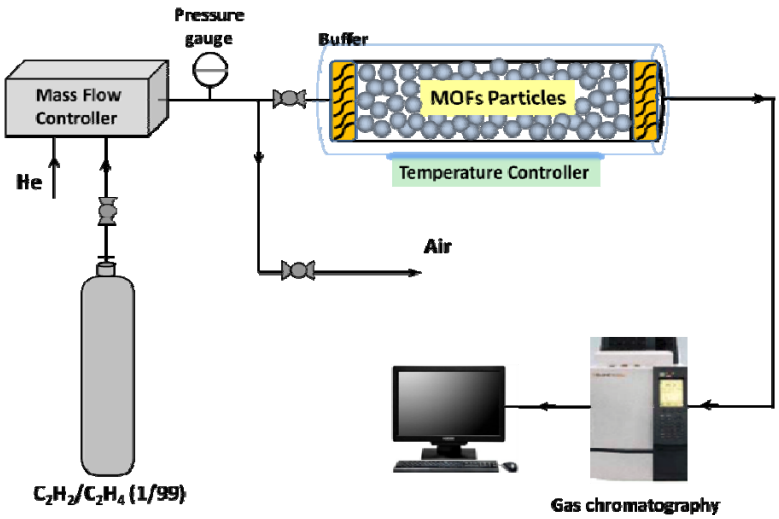

Figure S9. Breakthrough experiment apparatus.

Sample information in breakthrough experiment:

Length of adsorption bed: L = 150 mm

Inner diameter of adsorption bed: φ = 6 mm

Density of sample: 0.472 g/cm3

Total flow: 2 mL/min

Temperature: 298 K

Total pressure: 1 bar

weight of MOF powder 1.547 g

GCMC simulation and Density Functional Theory Calculations. All the grand canonical Monte Carlo (GCMC) simulation and density functional theory (DFT) calculations were performed by the Materials Studio 5.5 package. The adsorption sites of C_2H_2 and C_2H_4 at 298 K were obtained from GCMC simulations through the fixed loading task in the Sorption module. The host framework and the guest molecules were both regarded as rigid. The simulation box consisted of four unit cell and the Metropolis method based on the universal forcefield (UFF) was used. The Q_{Eq} derived charges and the ESP charges derived by DFT were employed to the host framework and guest atoms, respectively. The cutoff radius was chosen as 15.5 Å for the LJ potential, and the equilibration steps and production steps were both set as 5×10^6. All the geometry optimizations and binding energies were calculated by the density functional theory (DFT) method with periodic boundary through the Dmol^3 module. The widely used generalized gradient approximation (GGA) with the Perdew-Burke-Ernzerhof (PBE) functional and the double numerical plus d-functions (DND) basis

set were used. An accurate DFT Semi-core Pseudopots (DSPP) was employed for the metal atoms. Considering that a real description of the small molecule adsorption can only be obtained from an appropriate balance of all interactions, the DFT including the long-range dispersion correction (DFT+D) was taken into account using the Grimme (G06) semiempirical method to describe the long-range van der Waals interactions. For all the DFT calculations, the energy, gradient and displacement convergence criterions were set as 1×10^{-5} Ha, 2×10^{-3} Å and 5×10^{-3} Å, respectively.

We first optimized the Ni-DCPTP structures. C_2H_2 gas molecule was then introduced to the optimized Ni-DCPTP structure at the at the GCMC-identified adsorption site, followed by a full structural relaxation. To obtain the gas binding energy, a gas molecule placed in a supercell with the same cell dimensions was also relaxed as a reference. The static binding energy (at T = 0 K) was then calculated using $E_B = E_{(\text{Ni-DCPTP + gas molecule})} - E_{(\text{Ni-DCPTP})} - E_{(\text{gas molecule})}$.

Table S1. Breakthrough calculations for separation of C_2H_2/C_2H_4 mixture containing 1 mol% C_2H_2 at 298 K. The product gas stream contains less than 40 ppm C_2H_2.

	Dimensionless breakthrough time τ_{break}	Amount of C_2H_2 captured (mmol L^{-1})	Productivity of pure C_2H_4 (mol L^{-1})
M'MOF-3a	58.5	70	6.6
UTSA-100a	112.4	136	11.8
Ni-DCPTP	142	174	12.9

References

(1) Krishna, R.; Baur, R. Modelling Issues in Zeolite Based Separation Processes. *Sep. Purif. Technol.* **2003**, *33*, 213–254.